Analysis and Design of a Condensed Buck-boost Converter Utilizing Monolithic Bidirectional GaN Switches

Aklilu Aron, *Student Member, IEEE,* Paulin Eliat-Eliat, *Student Member, IEEE,* Justin Buonato, *Student Member, IEEE,* and Samantha Coday, *Member, IEEE*

***Abstract*—Many next-generation power converters require wide-range operation, capable of bidirectional power flow combined with buck and boost mode operation; thereby, supporting integration of renewable energy sources and storage on the grid and within electric drivetrains. This work presents a family of condensed buck-boost (CoBB) converters which utilize novel monolithic bidirectional switches (MBDS) to increase utilization of switches and passive components compared to conventional approaches. Moreover, multilevel CoBB converters are explored, showcasing their potential for dramatically reduced passive component requirements. The operation of the proposed converters is presented and fundamental comparisons in loss mechanisms and passive component sizing showcase the potential improvements. Moreover, a return path inductor variant is introduced to further reduce passive component requirements. Experimental hardware is presented showcasing operation of the two-level and three-level CoBB converter validating the theoretical analysis. Finally, control strategies for regulation and unity conversion ratios are provided and validated with the hardware prototype.**

I. Introduction

As industries across the world undergo rapid electrification, the design and implementation of dense and efficient power conversion becomes paramount to achieving a more renewable future. Modern power systems increasingly integrate variable power sources and electrical loads, such as batteries and solar or fuel cells, necessitating efficient power conversion over a wide regulation range. Many applications require a converter capable of buck and boost mode operation to achieve the optimal bus voltage. Examples include connecting photovoltaic strings to batteries or a regulated dc bus [1], battery systems in hybrid electric vehicles [2], and fuel cell powered adjustable speed drives [3]. Often these systems also require bidirectional power flow, enabling charging and discharging through a single converter. Therefore, developing flexible power converters with bidirectional flow, high conversion ratios, and efficient step-up and step-down voltage capabilities is essential for a sustainable future.

While many applications benefit from efficient and wide operating ranges, electric aircraft drivetrain are rapidly evolving and necessitate high specific power and efficiency for implementation. These aircraft vary in technology and degree of electrification, ranging from traditional aircraft with electrified auxiliary equipment to aircraft with all-electric propulsion [4]. Across these different implementations, there is a consistent need for power converters to serve as the interface between the energy storage (i.e. battery, hydrogen fuel cell) and the main distribution bus. Since operating conditions can vary in terms of battery voltage [5] and bus voltage [4], it is often desirable for the converter to be capable of both buck and boost functionality. Moreover, in many of these applications, bidirectional power flow is required to enable the charging and discharging of batteries through a single converter. The multilevel condensed buck-boost (ML-CoBB) converter, pictured in Fig. 1, comprises the main focus of this work and aims to address these challenges.

Buck-boost functionality can be achieved through many different converter topologies. The non-inverting buck-boost (NIBB) converter, shown in Fig. 2, is a common conventional approach. There are several ways the NIBB converter can be controlled; in this work, the NIBB converter is assumed to be operated such that two of four switches are always clamped on or off such that the topology resembles a buck or boost converter. This method of control is commonly used for high efficiency operation [6]. Thus, the NIBB converter represents a more conventional, magnetics-based approach to buck-boost conversion that is useful for comparison.

The flying capacitor multilevel (FCML) converter [7] is a hybrid switched-capacitor converter which utilizes capacitors for part of the energy conversion process, taking advantage of their higher energy density as compared to purely inductive converters [8]. The FCML converter also reduces the switch voltage stresses while maintaining a small inductor to allow regulation across varying output voltages and soft charging of the flying capacitors. Previous work [9], [10] has demonstrated buck-boost capability with the FCML converter by combining a buck FCML stage and boost FCML stage via a shared central inductor. This topology, shown below in Fig. 3 will be referred to here as the multilevel flying-capacitor buck-boost (ML-FCBB) converter and has been shown to achieve high power density and efficiency [10] compared to the conventional NIBB converter due to the decreased passive volume and switch stress.

Similar to the NIBB converter, the ML-FCBB converter can be controlled with several different methods. One approach involves clamping the appropriate redundant switches on or off. For the 3-level variant shown in Fig. 3, clamping S_3'

Aklilu Aron, Justin Buonato and Samantha Coday are with the Department of Electrical Engineering and Computer Science, Massachusetts Institute of Technology, Cambridge, MA 02139 USA.

Paulin Eliat-Eliat is with the Louvain School of Engineering at UCLouvain, Belgium.

Corresponding author: Samantha Coday (coday@mit.edu)

DOI: 10.1109/TPEL.2025.3604743

TABLE I: Topology Comparison

Topology	# Inductors	# Flying Caps	# MBDS	# Unipolar Switches	Constraints
NIBB	1	0	0	4	-
ML-FCBB	1	$2(N-2)$	0	$4(N-1)$	capacitor balancing
CoBB	2	0	1	2	-
ML-CoBB	2	$N-2$	$2(N-1)$	2*	-
RPI-CoBB	1	0	1	2	common-mode voltage
RPI-ML-CoBB	1	$N-2$	$2(N-1)$	2*	common-mode voltage

*As described in Section II, unipolar switches can be used to replace some of the MBDS, for specific conversion ratio ranges.

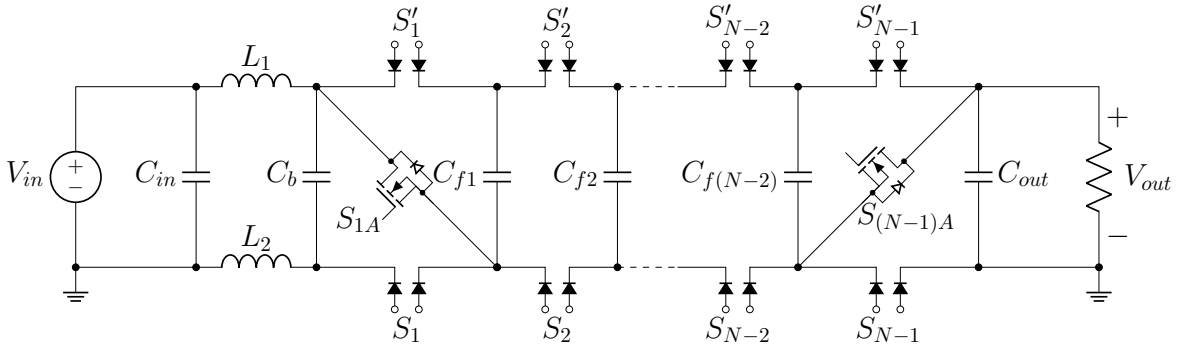

Fig. 1: N-level multilevel condensed buck-boost (ML-CoBB) converter.

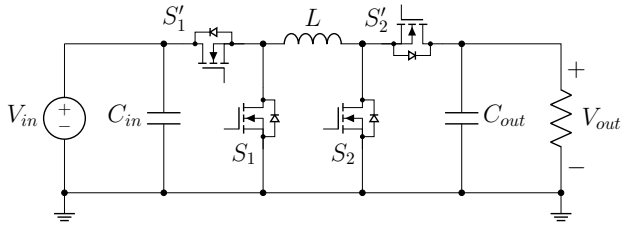

Fig. 2: Non-inverting buck-boost (NIBB) converter.

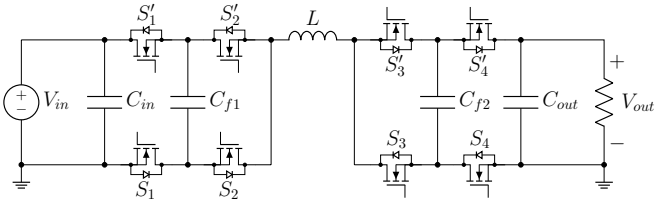

Fig. 3: 3-level multilevel flying-capacitor buck-boost (ML-FCBB) converter.

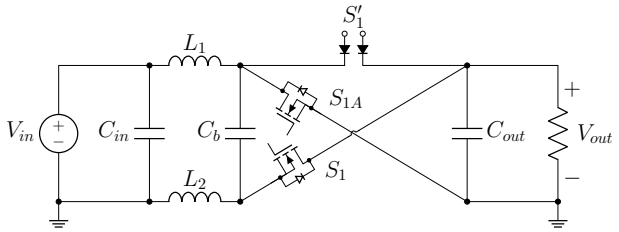

Fig. 4: Condensed buck-boost (CoBB) converter.

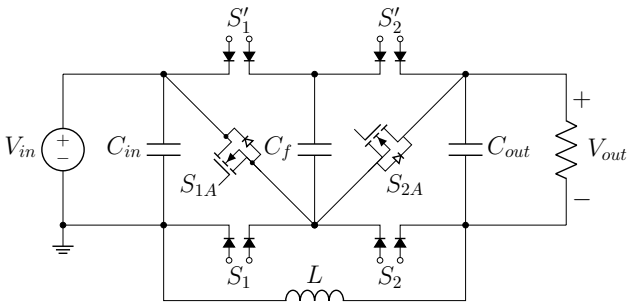

Fig. 5: 3-level RPI CoBB converter.

and S'_4 on and opening S_3 and S_4 results in the same topology as the buck FCML converter. Alternatively, clamping the switches to the left of the inductor would enable boost functionality. While this operation of the ML-FCBB converter successfully pairs buck-boost operation with the benefits of the FCML topology, it has some key redundancies that limit efficiency and density. Clamping switches off means that there are FETs and accompanying gate power and drive circuitry taking up board space and weight, while not actively contributing to power conversion. Switches clamped on not only have the same challenges, but also introduce additional conduction losses, impacting efficiency. It is important to note that while higher level counts are often desirable to improve performance by shifting even more energy processing to the capacitors, this would only further exacerbate the challenge of redundancy due to the mirrored nature of the topology requiring four additional switches for every increase in level count. Similarly, the mirrored design requires two flying capacitors for each increase in level count, where half are always unused, resulting in poor passive component

utilization. Additionally, the unused capacitors are left floating and charge or discharge upon switching between buck and boost mode unless a more complicated control scheme is used to actively balance all of the flying capacitors, as demonstrated in [9]. These challenges motivate the exploration of a topology that can achieve efficient buck and boost conversion in a more condensed topology, eliminating the redundant devices. The converters featured in this work, termed the condensed buck boost (CoBB) converter (Fig. 4), and multilevel condensed buck boost (ML-CoBB) converter (Fig. 1), achieve this by utilizing a split-inductor approach and the incorporation of novel, monolithic bidirectionally blocking switches.

This work explains the operation of the ML-CoBB converter, focusing on the parts of the topology that vary from the typical FCML converter, and expanding on [11], where the ML-CoBB topology was first presented as the non-mirrored buck boost converter. A theoretical framework is presented to compare the benefits of the ML-CoBB topology to that of the ML-FCBB converter as well as the conventional, magnetics-based NIBB converter. Next, a hardware prototype for the ML-CoBB converter is presented and evaluated against a similarly specified NIBB converter to validate the theoretical conclusions. A variant of the ML-CoBB topology that uses only one inductor in the return path is also explored, and finally, an initial control scheme for the ML-CoBB converter is presented and verified.

II. Converter Design and Operation

To understand the ML-CoBB converter in Fig. 1, it is helpful to start with the basic building block of the proposed family of topologies, the CoBB converter as shown in Fig. 4. This topology builds on the input-inductor buck converter [12], or split-inductor buck converter, which allows for buck operation with inductors at the input instead of output, splitting them across the high and low sides to ensure constant current flow. This input inductor buck has been used in several applications [13], [14] to potentially improve filtering and allow for easier packaging of inductors off-chip [15]. As shown in Fig. 6(a), when the CoBB converter operates with switch S_{1A} clamped off, the topology is equivalent to the input inductor buck converter. Alternatively, when switch S_1 is clamped off, the converter resembles a conventional boost converter with an additional inductor L_2, which has zero average current flowing through it. Therefore, this topology has the ability to operate as both a buck and boost converter by selecting which switches operate in either mode. Note, as discussed in Section II-C, this topology requires a bidirectionally blocking switch, S_1' to operate in both modes.

Similar to how the buck converter can be made into the FCML converter by adding pairs of switches and flying capacitors, so can the CoBB converter. The resulting generic N-level ML-CoBB converter is shown in Fig. 1. As shown in the following analysis, the ML-CoBB converter decreases component count compared to the ML-FCBB converter and decreases passive component sizing compared to the NIBB converter, resulting in a good candidate for dense and efficient buck-boost conversion.

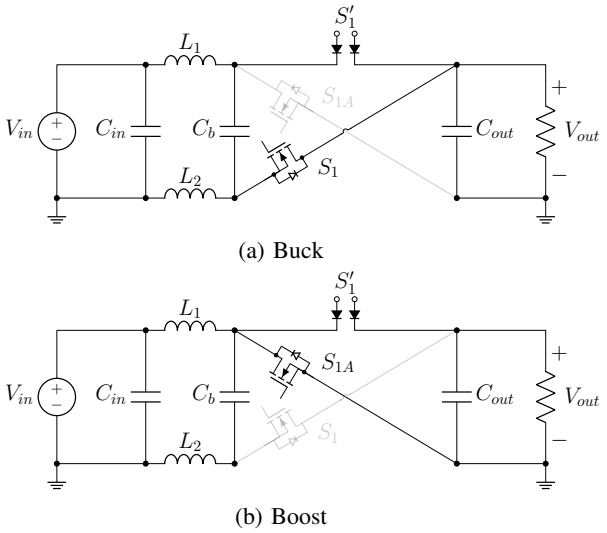

(a) Buck

(b) Boost

Fig. 6: Buck and boost configurations for the (2-level) CoBB converter.

Aside from the new aspects of the topology that will be detailed below, the ML-CoBB converter's operation and control is much like that of a standard FCML converter. In this work the converter is operated far above resonance to reduce current stress on the inductors and allow for output voltage regulation. This is a design choice; the converter could alternatively utilize a different control scheme that operates at resonance with a fixed conversion ratio. The switch gates are controlled via a phase-shifted PWM scheme, with two additional switches clamped off in either mode of operation. Fig. 7 shows how disabling the appropriate switches can create a circuit much like the buck or boost FCML converters. While there are still two unused switches, there are no redundant conducting switches. More importantly, the clamped-off switches are constrained to one at the input and one at the output of the converter, resulting in no increases in unused switches with level count (the middle chain of flying capacitor and switch cells shown in Fig. 1 is the same for both buck/boost operation). As with most conventional FCML converters, the flying capacitors will balance to voltage multiples of $\frac{V_{max}}{N-1}$[1], ranging from $\frac{V_{max}}{N-1}$ to $\frac{(N-2)V_{max}}{N-1}$. As a result, the voltage blocked by each switch is $\frac{V_{max}}{N-1}$, excluding capacitor ripple.

A. Split Inductors

The inductor current ripple is the same in both L_1 and L_2, and follows from the ripple for the standard FCML converter:

$$\Delta i_L = \frac{V_{max}(1-D_{eff})}{L(N-1)^2} D_{eff} T, \tag{1}$$

where $L = L_1 = L_2$ and D_{eff} is the effective duty cycle (as defined in [16]):

$$D_{eff} = (N-1)D - \lfloor (N-1)D \rfloor. \tag{2}$$

[1] V_{max} and I_{max} represent the maximum of the two (input and output) parameters for the topology of interest. For example, the ML-CoBB converter in buck mode has $V_{max} = V_{in}$ and $I_{max} = I_{out}$.

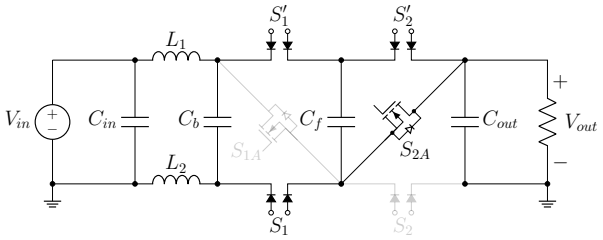

(a) Buck

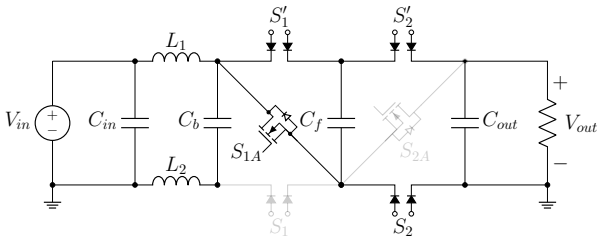

(b) Boost

Fig. 7: Buck and boost configurations for a 3-level ML-CoBB converter.

It should be noted here that this work uses the convention of defining D to be the duty cycle of the high-side switches for buck mode (S_x'), and that of the low-side S_x for boost mode.

Both the CoBB converter and ML-CoBB converter utilize split inductors. These inductors can be placed at the converter's input, output, or at both locations. Depending on the system and desired application there may exist benefits to placing the inductors on one terminal over the other. For simplicity the inductors are placed at the input for the remainder of the work; however, the analysis and results can be easily applied to an output inductor converter.

Moreover, L_1 is chosen to be equal to L_2 in this work for simplicity, but that is not necessary. Previous work, [13] demonstrating an input inductor FCML converter, sizes the inductors to maintain a constant ripple ratio which results in two different inductor values. Equation (1) is very similar to that of a buck or boost converter, except for the use of D_{eff} instead of D, and the $(N-1)^2$ term in the denominator. This term represents the benefits of the FCML topology, where one of the $(N-1)$ terms comes from the reduced voltages exposed to the inductors, and the other $(N-1)$ accounts for the higher effective frequency that results from the phase-shifted PWM. This energy that would previously have been processed via higher inductor ripple and volume is instead processed by the flying capacitors.

Split inductor buck converters [17] have been designed for a number of applications. Previous work, [18], makes use of a current-source input buck topology to step down voltage while maintaining a smooth input. Rather than just an EMI feature, the split-inductor is necessary for the ML-CoBB converter. This requirement exists because, during buck mode operation, there must be a path for dc current to flow that does not include the input (equivalent to the freewheeling state in the conventional buck converter).

The split inductors ensure that there is always an inductor in the path of current flow to enable the soft-charging characteristic of hybrid switched capacitor converters. In buck mode, the average current is split among both inductors such that L_1 has an average current of DI_{out} and L_2 has average current $(1-D)I_{out}$. In contrast, since the standard boost FCML converter has an input inductor, L_2 does not carry any average current in boost mode, though it does ripple around zero amps.

The use of the split-inductor approach requires a capacitor C_b that connects the two inductors to the switch network. This is especially critical in buck configuration, because there is a state where S_1 is open. During this state, since inductor current cannot be discontinuous, the current and energy stored in L_2 has to go through C_b to get to the output. The charge built up on C_b is then discharged when current conducts in the reverse direction in the following state. In periodic steady state, the average voltage across the inductors is 0 V. Thus, C_b will have an average voltage of V_{in} and can be sized according to ripple requirements.

B. Return Path Inductor Variant

A variant of the proposed topologies is shown in Fig. 5. This topology, the Return Path Inductor (RPI) CoBB, uses an RPI, similar to the Y-inverter presented in [19]. This variant requires only one inductor, resulting in half the required inductance for equal inductor ripple compared to the ML-CoBB converter. However, the RPI introduces high-frequency common-mode voltage between the input and output (equal to v_L at the effective frequency), limiting the potential applications to those which do not require a common-ground reference. For example, previous work [19], has utilized RPI-type converters for motor drive applications. This converter can be designed as a two-level converter, the RPI-CoBB converter. The RPI-CoBB can also be extended to a multilevel variant, the RPI-ML-CoBB converter, taking advantage of higher-level counts for decreased inductor volt-second requirements, similar to the conventional FCML converter.

C. Bidirectional Switches

As described above, the ML-CoBB topology requires switch implementations that have bidirectional blocking capability. This has been done in previous work by pairing two, antiseries FETs [20], but this approach doubles the number of switches, subtracting from the benefits achieved by the condensed topology through increased switch area and gate drive complexity. The recent development of monolithic, bidirectional switches (MBDS), also known as four quadrant or ac switches, offers single devices that make use of wide-bandgap technologies such as GaN [21], [22] or SiC [23], [24], and provide the desired reverse blocking characteristics integrated onto one, monolithic piece of semiconductor, alleviating the issues with the two switch approach above. Recent work utilizing MBDS has shown potential improvements in current-source inverters [21], [25] and single-stage single-phase rectifiers [26].

While these devices open up exciting new topologies, they are still in the early stages of production and may not be able to match the performance metrics of industry standard single GaN FETs. For this reason, it is worthwhile to discuss which

of the switches in the ML-CoBB design must be bidirectional, and which can be unipolar. As previously mentioned, most of the switches have to be bidirectional as they are being used in both directions for buck and boost mode. Intuitively, this can be seen by overlaying a buck and boost FCML converter on each other, and observing that the body diodes for each overlapping FET point in opposite directions. However, since there is no direct overlap for the two pairs of bottom-corner switches S_{1A}, S_1, $S_{(N-1)A}$, and S_{N-1} (this is the reason two of them are always clamped off), they are potential candidates for unipolar switches. By comparing the voltages in each state (Table II), it can be shown that the diagonal switches S_{1A} and $S_{(N-1)A}$ can be unipolar. The bottom two, S_1 and S_{N-1}, represent a more interesting case, whereby they can be unipolar so long as extreme duty cycles are avoided. Specifically, if buck mode $D < \frac{1}{N-1}$ or boost mode $D > \frac{N-2}{N-1}$, switch S_{N-1} or S_1 respectively will reverse conduct. Considering the flying capacitor ripple adds further complexity, as with high enough capacitor ripple, reverse conduction can occur without entering the extreme duty cycles. The more complete expression for those two cases would be:

$$v_{S_{N-1}} = V_{out} - \frac{V_{in}}{N-1} + \Delta v_{C_f} \tag{3}$$

$$v_{S_1} = -(V_{in} - \frac{V_{out}}{N-1} + \Delta v_{C_f}), \tag{4}$$

with the expression for Δv_{C_f} given below. The equation for voltage ripple includes a new term D^*. The piecewise function for D^* given in (6) arises from the fact that Δv_{C_f} depends on the time a given flying capacitor is charging, which is a function of both duty cycle and level count, and the manner in which adjacent switching cells overlap.

$$\Delta v_{C_f} = \frac{I_{max}}{C_f} D^* T \tag{5}$$

$$D^* = \begin{cases} D & D \leq \frac{1}{N-1} \\ \frac{1}{N-1} & \frac{1}{N-1} \leq D \leq \frac{N-2}{N-1} \\ 1-D & D \geq \frac{N-2}{N-1}. \end{cases} \tag{6}$$

Therefore, if the converter operating ranges are well known before designing, additional efficiency and complexity improvements may be possible by selecting the maximum number of unipolar FETs.

III. Losses and Passive Weight Comparisons

The ML-CoBB converter is motivated by its potential for high power density compared to conventional non-inverting buck-boost topologies. To discuss these ideas from a theoretical perspective, it is useful to introduce figures-of-merit (FOMs) that describe the losses in terms of key circuit parameters. As previously mentioned, the NIBB converter is always assumed to be in a clamped state such that it topologically equivalent to a buck or boost converter.

A. Switch Losses

The losses in the switches can be broken down into two categories: conduction losses and switching losses. The conduction loss FOM, M_C, can be described as follows:

$$M_C = \frac{1}{I_{max}^2} \sum_k I_{ds,k}^2, \tag{7}$$

where I_{ds} represents the current through the switch while it is conducting, and k represents number of switches in a possible conducting path. Note that the sum is normalized using the maximum current (I_{in} or I_{out}). Since all the converter topologies discussed here always have either I_{in} or I_{out} conducting through any switch, M_C corresponds to the number of switches in the conducting path.

Figure 8 shows the value of M_C for each of the converters described in this work. The NIBB converter has double the calculated M_C compared to the CoBB converter due to the latter's reduced number of switches. Similarly, since M_C scales with the number of switches (N-1), the ML-FCBB variant has double the M_C compared to the ML-CoBB converter, and this trend continues as level count increases. To allow for generalization, this FOM does not account for different switch $R_{ds,on}$ values. This means the trends presented here may vary with switch implementation, especially if there are dramatic differences in parameters like $R_{ds,on}$. Relevant factors include the anticipated increase in $R_{ds,on}$ for MBDS and expected decrease in $R_{ds,on}$ for lower voltage switches enabled by multilevel topologies. Section II presented the two special switches S_{1A} and $S_{(N-1)A}$ which could always be implemented with unipolar devices due to a consistent blocking voltage polarity. However, these two switches must block the full V_{in} or V_{out} (Table II), which could result in less favorable $R_{ds,on}$ or device scaling; thereby, impacting the switch selection and expected losses. Note that these are the only two switches with this feature, meaning this effect is less pronounced as level count increases.

Switching losses can be approximated by:

$$M_S = \frac{1}{P} \sum_n V_{ds} I_{ds}, \tag{8}$$

where V_{ds} is the voltage blocked by a switch when it is off, n is the number of switches, and P is the power processed by the converter ($V_{in}I_{in} = V_{out}I_{out}$). The switching loss FOM, M_S, for the NIBB converter is equal to $\frac{2}{D}$ in buck mode, and $\frac{2}{1-D}$ in boost mode, reflecting the increased stress at more extreme conversion ratios. Despite having one less switch, the CoBB converter has the same M_S due to the fact that the clamped-off switch doesn't contribute to switching losses. Importantly, the ML-CoBB converter also shares the same M_S (regardless of level count) because, despite having a multiple of (N-1) more switches, the reduction in blocking voltage due to higher level count decreases the FOM by the same factor of (N-1). Once again, even though the ML-FCBB converter has many redundant switches, it too shares the same M_S due both to lower blocking voltages and half of the switches being clamped on ($V_{ds} = 0$) or off ($I_{ds} = 0$). Thus all four topologies have the same M_S metric, but the multilevel

Switch	Buck	Boost
Top	$\frac{V_{in}}{N-1}$	$-\frac{V_{out}}{N-1}$
Bottom	$-\frac{V_{in}}{N-1}$	$\frac{V_{out}}{N-1}$
$\boldsymbol{S_{1A}}$	$\frac{N-2}{N-1}V_{in}$, V_{in}	$\frac{V_{out}}{N-1}$
$\boldsymbol{S_1}$	$-\frac{V_{in}}{N-1}$	$-(V_{in}-\frac{V_{out}}{N-1})$, $-V_{in}$
$\boldsymbol{S_{(N-1)A}}$	$-\frac{V_{in}}{N-1}$	$-\frac{N-2}{N-1}V_{out}$, $-V_{out}$
$\boldsymbol{S_{N-1}}$	$(V_{out}-\frac{V_{in}}{N-1})$, V_{out}	$\frac{V_{out}}{N-1}$

TABLE II: Voltage blocked by switches in the off state, according to position and operating mode. Positive voltage is defined from right to left as drawn in Fig. 1, and entries with multiple expressions represent switches with two different off-states (e.g. the voltage blocked by S_1 when S_1' is conducting vs when S_{1A} is conducting).

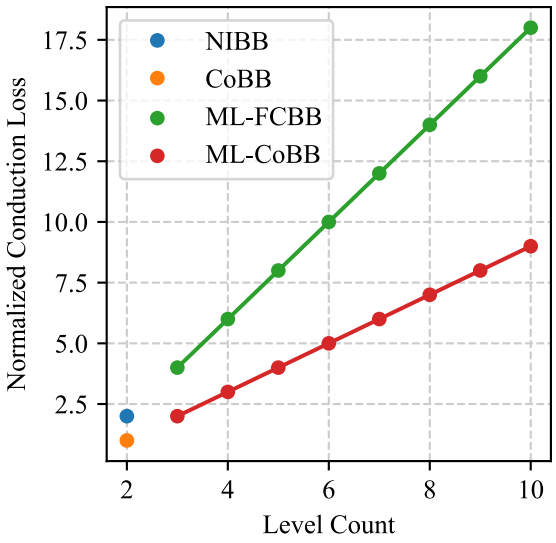

Fig. 8: Switch conduction loss FOM, M_C, for the NIBB, CoBB, ML-FCBB, and ML-CoBB converters as a function of level count, N.

topologies may yet offer benefits related to switching loss in the sense that a higher number of lower-rated devices may be more favorable [27].

B. Inductor Losses

Inductor-related losses can be broken down into two categories: dc losses (related to DCR) and ac losses (core hysteresis, eddy currents, etc.).

A reasonable FOM for the ac losses involves the inductor ripple:

$$M_L = \frac{1}{\Delta i_{L,0}} \sum_n \Delta i_L, \tag{9}$$

where n is the number of inductors in the converter, and $\Delta i_{L,0}$ is the inductor ripple for the 2-level converter in the respective configuration. This normalization means that $M_L = 1$ for the NIBB converter and $M_L = 2$ for the CoBB converter in either buck or boost mode. Using the standard FCML inductor ripple equation (1), the ML-FCBB converter has $M_L = \frac{1}{(N-1)^2}$. In this case, the ML-CoBB converter has higher anticipated ac losses at $M_L = \frac{2}{(N-1)^2}$ since the two inductors are exposed to the same voltage differentials. For both the ML-FCBB and ML-CoBB converters, increasing level count results in a rapid drop in ripple-related losses. This can be visualized in Fig. 9, where M_L is related to the peak of each curve. These ripples apply to all converter topologies discussed in this work: $N = 2$ accounts for the NIBB and CoBB converters, while the higher level counts are applicable to the ML-FCBB and ML-CoBB converters. The shape is the same for both buck and boost operation, assuming proper normalization with the corresponding 2-level case (i.e. NIBB converter in boost mode). Ripples are also the same for RPI variants because the voltages applied to the inductor(s) do not change, although M_L would be smaller due to one less inductor.

The dc losses are the same for all converters discussed here because the summed average inductor currents are equal across each topology. Notably, despite the presence of two inductors in the split-inductor CoBB converters, the current is shared between them as explained in Section II such that dc losses should be roughly equivalent. However, just like for switch conduction losses, M_L does not account for differences in inductor DCR. Future works may explore the multivariate relationship between level count, losses, and how smaller inductor requirements may affect this via different device parasitics, including the known trend of several smaller inductors leading to higher losses, compared to a single large inductor [28].

Considering the FOMs together, it is clear that the CoBB converters tend to either match or outperform their existing counterparts. M_C and M_L demonstrate how the condensed topology shines in terms of minimizing losses at higher level counts. M_S and the dc inductor losses are consistent across all four topologies. While it is important to take into account practical device parameters when looking for very specific comparisons, the FOMs presented here indicate promising trends in favor of the CoBB topologies.

C. Passive Weight

The previous sections detailed the benefits of the ML-CoBB converter in terms of losses. Another key advantage comes from the improved utilization of components, both active and passive. As shown in Fig. 8, the condensed topology cuts down on the number of required switches when compared with the ML-FCBB converter. This has the effect of reducing

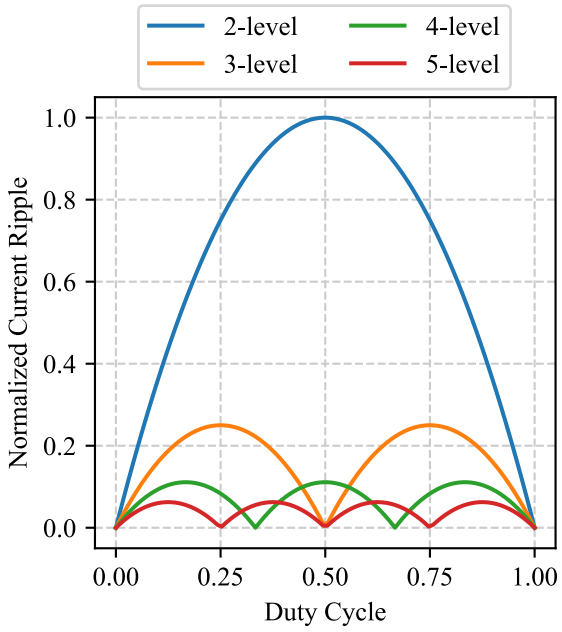

Fig. 9: Current ripple, Δi_L, for different level counts, plotted against duty cycle. Normalized to the ripple in the 2-level variant (i.e. NIBB or CoBB converter).

conduction losses, and the impact becomes more dramatic as level count increases. In addition to less power loss, the absence of redundant switches and associated gate driver circuitry results in less converter weight for the same power processing capability. Similarly, for each redundant switching cell *condensed* by the ML-CoBB topology, there is also one less flying capacitor than in the ML-FCBB converter. The comparison to the ML-FCBB converter highlights the ML-CoBB converter's enhanced utilization, and turning to comparisons with the NIBB converter further demonstrates the benefits related to passive weight.

One of the powerful features of the FCML topology is the ability to shift some of the converter's energy processing from the inductor onto the flying capacitors. As a result, since capacitors have more favorable energy densities [8], the overall converter power density can be improved. This concept is formalized by writing analytical expressions for the voltages and currents in the circuit, and using them to determine the maximum energy that must be stored in the passive components. Then, approximate gravimetric energy density values can be used for each category of passive elements to convert that to a minimum passive weight. Here, the NIBB converter and ML-CoBB converter will be compared in terms of their required passive weight for the same amount of energy processing. The decision to compare weights is based on the intended application in electrified aircraft, for which weight optimization is paramount. However, this analysis can be carried out for volume comparisons by using an energy per volume density instead. To account for the split inductors, the analysis for the ML-CoBB converter is carried out assuming an FCML buck or boost design (with one inductor), then the final inductor weight result is multiplied by two. Since the current sharing between L_1 and L_2 depends on duty cycle, the inductors cannot be separately optimized; rather they must be sized such that they could both take the full current stress, hence treating it as a single inductor FCML converter and doubling the result. This method is acceptable because from the perspective of passive components, the ML-CoBB converter is equivalent to a buck or boost FCML converter, excepting only the extra inductor.

Since the NIBB converter operation involves clamping into a buck or boost mode, the inductor average current and ripple current match that of the standard form of those converters. Taking buck mode as an example, the average current $I_L = I_{out}$, and the ripple current $\Delta i_L = \frac{V_{out}(1-D)D}{f_{sw}L}$. For an FCML buck converter, I_L would be the same, but Δi_L would be smaller by a factor of $\frac{1}{(N-1)^2}$, following from (1). For the purposes of comparing inductor energy between the two converters, it is useful to rewrite the ripple equation in terms of the minimum inductance required for a certain ripple:

$$L_{NIBB} = \frac{V_m(1-D)D}{f_{sw}\Delta i_L} \tag{10}$$

$$L_{CoBB} = \frac{V_m(1-D_{eff})D_{eff}}{f_{sw}\Delta i_L(N-1)^2}, \tag{11}$$

From there Δi_L can be chosen based on desired inductor loss, inductor size, and soft-switching requirements. This reference can then be used to determine what value of L would be required for either converter to meet this ripple requirement. Specifically, this is the value of L for which the ripple in the worst-case current situation is equal to the chosen ratio of I_{max}. Then, both inductors must be sized for this L (because of asymmetric current sharing in buck mode). Note that this is different from some other approaches, such as in [13], where the split inductors have different inductances but a constant ripple ratio.

The peak energy in the inductor and capacitors are as follows:

$$E_L = \frac{1}{2}L(I_L + \frac{\Delta i_L}{2})^2 \tag{12}$$

$$E_C = \frac{1}{2}C(V_{Cf} + \frac{\Delta v_{Cf}}{2})^2. \tag{13}$$

Considering the passives that contribute to energy processing (excluding bulk capacitance), the NIBB converter has only its inductor. The ML-CoBB converter has both inductors and the flying capacitors, and the weight of the latter must also be considered for a complete picture.

Comparing the passive energy for the NIBB and ML-CoBB converters results in the ratio shown in the first line of (14). Due to the fact that this specific design includes a high capacitor-to-inductor energy density ratio and constrains ripple, the weight due to flying capacitor energy processing is dwarfed by that of the inductors [8]. Under these conditions, the ratio simplifies nicely to the result in (14).

$$\begin{aligned}\frac{E_{P,NIBB}}{E_{P,CoBB}} &= \frac{E_{L,NIBB}}{E_{L,CoBB}+E_{C,CoBB}} \\ &\approx \frac{(1-D)D}{(1-D_{eff})D_{eff}}(N-1)^2.\end{aligned} \tag{14}$$

The passive weight comparison between the NIBB and ML-CoBB converters is shown in Fig. 10. Due to the multilevel design and phase-shifted PWM, the ML-CoBB converter has specific duty cycles for which the inductors do not ripple at all. Those operating points represent the theoretical peaks for weight ratio because only the capacitors are considered for the ML-CoBB converter. However, given that the converter is intended to function with variable duty cycle in this application, the peaks of the curves are not as useful as the minimum values. Comparing the bottom of the curves for each level count reveals how increasing N offers dramatic improvement in weight ratio. The prototype discussed in this work, at $N = 3$, represents the least significant weight ratio, sitting between 2-3x across most duty cycles (see also Fig. 16). As level count increases, the minimum possible weight ratio quickly increases past 10x, even ignoring the much higher peaks at certain duty cycles. Thus, analyzing the two converters from a passive weight perspective demonstrates one intended aspect of the ML-CoBB converter: the ability to process power at much higher densities.

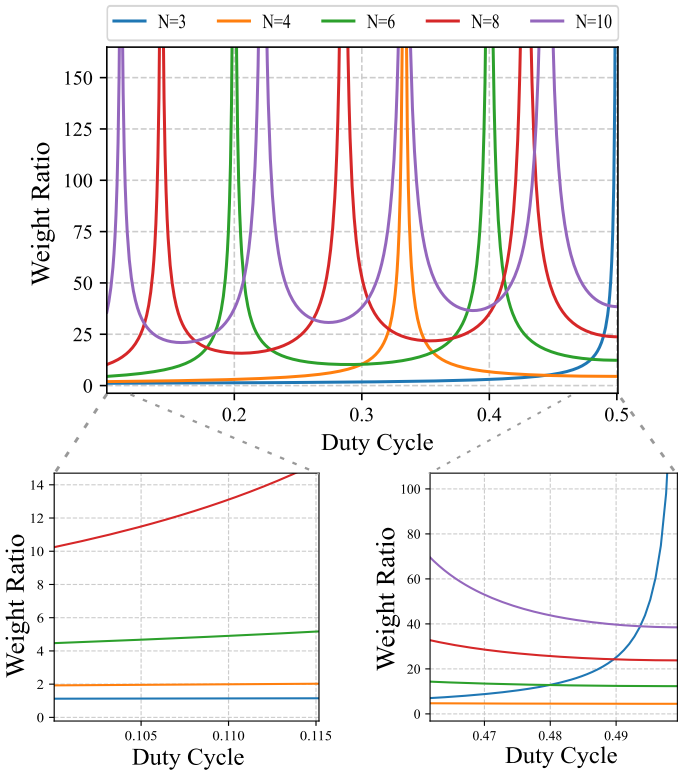

Fig. 10: Theoretical passive weight ratio of NIBB converter divided by ML-CoBB converter as a function of duty cycle, plotted for different level counts, N, following from (14). The duty cycle is shown up to 0.5 because it is symmetric above that point due to the effective duty cycle D_{eff}.

IV. Hardware Implementation and Evaluation

To demonstrate the functionality of the ML-CoBB converter, a 3-level hardware prototype was built and sized for a representative application in electrified aircraft. The operating conditions were selected from a survey of current and future electrified aicraft and can be seen in Table III [4], [29]. An input voltage range of 200 V to 500 V was chosen to represent variability in battery or fuel cell voltage, and to demonstrate the buck-boost operation. The prototype was designed to process at least 1 kW as an initial demonstration, though actual implementations would likely meet power requirements either by designing for higher power or parallelizing multiple converters. A frequency setpoint of 100 kHz was chosen to be far above resonance and keep ripple currents low, but not so high as to introduce excessive losses.

TABLE III: Prototype Specifications

Input voltage	200-500 V
Output voltage	270 V
Switching frequency	100 kHz
Power	1 kW

The bidirectional switches were realized using preliminary devices provided by Transphorm, and the unipolar switches were implemented using 650 V devices from GaN Systems. The switch voltage ratings are higher than necessary, both to account for component derating and limited availability. However, a key benefit of the multilevel ML-CoBB converter is the reduced switch stress; in this application the switches could have been rated for as low as 300 V (well below the input voltage), and perhaps taken advantage of the aforementioned favorable switch scaling at lower voltages. The flying capacitor was selected for voltage rating and minimal ESR, and a moderate capacitance to allow for acceptable voltage ripple (<20%). For the inductors, a script was used to search for inductor combinations that kept current ripples within allowable limits, and the options were plotted to compare their size and resistive losses, as show in Fig. 12.

The ML-CoBB converter prototype was assembled for testing as shown in Fig. 11. Figures 13(b) and 13(e) demonstrate successful operation via key circuit waveforms at 880 W in both modes. Note, the analysis presented in Section III assumes linear inductor current; however, as seen in Fig. 13(b), the inductor current is sinusoidal during several subphases, while operating in buck mode, due to C_b and the split inductor's resonant frequency. Nonetheless, the inductor ripple and average current measured in the hardware prototype closely match the analysis. The inductor currents i_{L_1} and i_{L_2} have approximately the same ripple, with the difference that i_{L_2} is centered around 0 A in boost mode but shared between i_{L_1} and i_{L_2} in buck mode. Note also that this sharing is almost even, as would be expected from a duty cycle of $D = 0.54$ based on the analysis in Section II-A.

Another check on the converter functionality is given by the v_{SW} waveforms. Since this is a measurement of the voltage at the node connecting L_1 and C_b, it alternates between showing information about the terminal voltages and the flying capacitor voltage. Though not a main focus of this work, the experimental v_{SW} waveforms indicate successful flying capacitor balancing, evident from the relatively consistent voltage pulses (e.g. in boost mode $v_{C_f} \approx \frac{V_{out}}{2}$). Due to the flexibility of the ML-CoBB topology, a modified version of

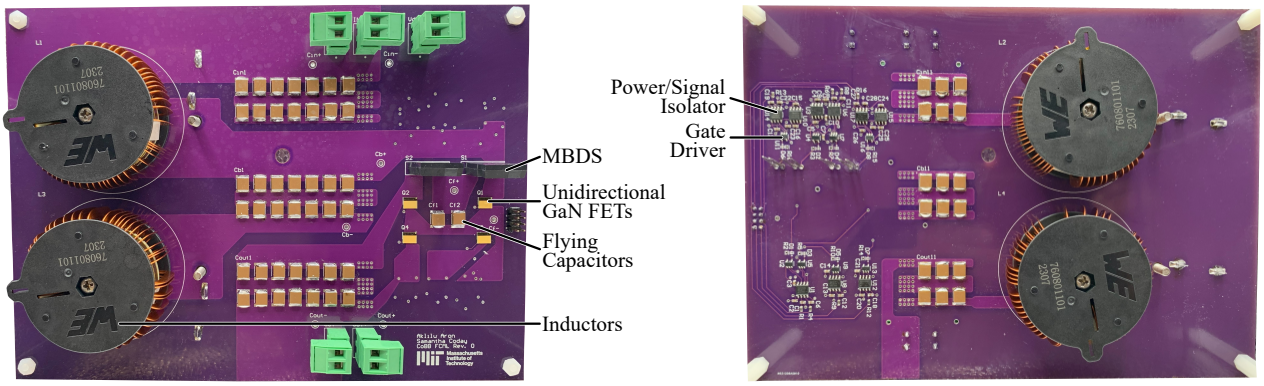

(a) (b)

Fig. 11: Labeled photographs of the (a) front and (b) back of the ML-CoBB prototype.

TABLE IV: Converter Components

Device	CoBB	NIBB
Bidirectional Switches	Transphorm TP65F060WS (Prelim), 650 V	-
Unidirectional Switches	GaN Systems GS66506T, 650 V	Anbon AS1M0040120T, 1200 V
Flying Capacitors	TDK C5750X6S2W225K250KA, (2 parallel) 2.2 μF	-
Inductors	Kemet MPX1D2213L680, 2x (2 parallel) 68 μH	Wurth 760801101, (2 parallel) 255 μH
Control	**MBDS**	**Unipolar**
Power/Logic Isolators	ADI ADuM5240 (2 series)	ADI ADuM5240
Gate Drivers	TI UCC44273	TI UCC44273

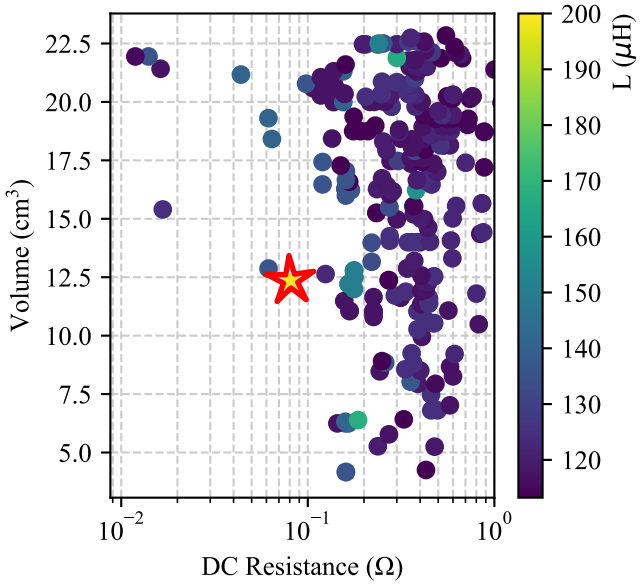

Fig. 12: Possible candidates for L_1 and L_2, with the selected inductor starred in red.

the (2-level) CoBB converter was also tested by clamping the appropriate switches. Figures 13(a) and 13(d) verify correct functionality at low power.

Efficiency measurements were gathered using a Yokogawa WT5000 power analyzer. The circuit was cooled with a small fan and efficiency measurements do not include gate drive losses. Figures 13(c) and 13(f) plot efficiency against power for both operating modes. Operation in boost mode is more efficient than buck mode, peaking around 97.5% compared to 95.4%. One explanation for this lies in the difference between duty cycles. Boosting from 200 V to 270 V corresponds to a duty cycle of $D = 0.26$, and is a far less extreme conversion than bucking from 500 V to 270 V at $D = 0.54$.

A. NIBB Converter Comparison

A NIBB converter was designed in tandem to represent a baseline for comparing the ML-CoBB converter's performance to a more conventional design. This converter was designed to the same specifications as the ML-CoBB converter, but the differences in topology detailed in Section II result in some different component selection. Two key examples include FETs that must be rated for higher voltage (no multilevel effect), and a larger inductor (no frequency multiplication). Furthermore, since the NIBB inductor was standardized to the same ripple requirements as the ML-CoBB inductors, the inductor must be even larger than 2x due to the fact that the NIBB converter has a higher ripple. Wherever possible, components were chosen with parameters to match the loss of those in the ML-CoBB ($R_{ds,on}$, C_{OSS}, etc).

The NIBB converter was tested at the same operating conditions as the ML-CoBB converter, and Table V summarizes the key results. The NIBB converter efficiencies follow the same trend as those of the ML-CoBB converter and are close in value. Section III presented a framework for comparing

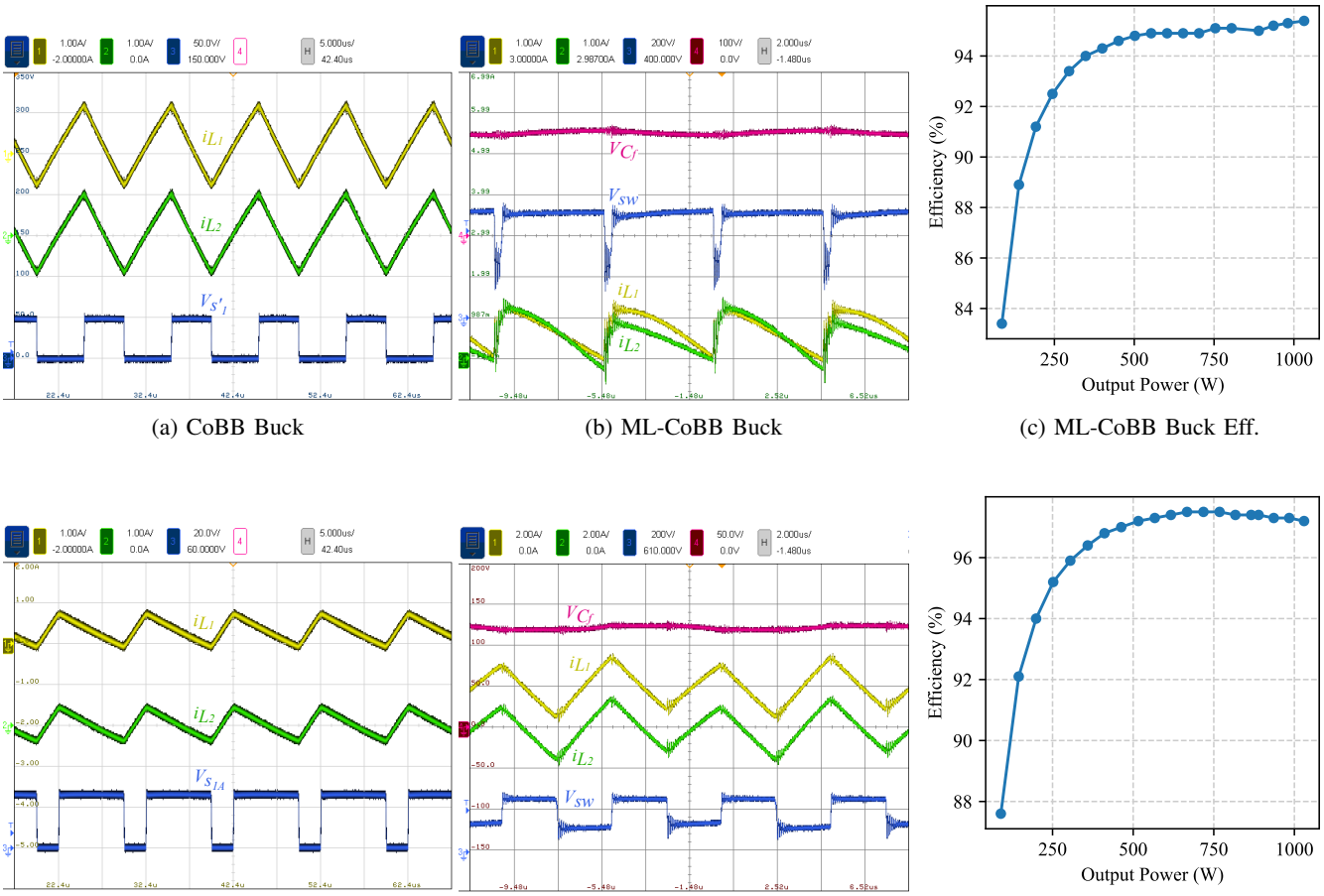

(a) CoBB Buck (b) ML-CoBB Buck (c) ML-CoBB Buck Eff.

(d) CoBB Boost (e) ML-CoBB Boost (f) ML-CoBB Boost Eff.

Fig. 13: Scope shots to verify operation of the various CoBB topologies. The ML-CoBB ($N = 3$) waveforms represent bucking from 500 V and boosting from 200 V, both to an output of 270 V at 880 W. The CoBB ($N = 2$) converter waveforms were tested at low voltage ($\frac{1}{10}$ of the multilevel version). The measured voltage v_{SW} is the voltage at the node connecting L_1 and C_b, referenced to ground.

the weights of the ML-CoBB and NIBB converters. Using the actual component weights (4x 34 g for ML-CoBB and 2x 194 g for NIBB) results in a NIBB to ML-CoBB weight ratio of 2.85, which is in the center of the blue $N = 3$ curve in Fig. 10, and shown in detail in Fig. 16. It is important to note that while the curves of Fig. 10 offer useful expectations for achievable weight ratios, they are not exact. Specific design decisions such as inductor current ripple, and the implementation/availability of passive components with different maximum ratings may affect final weight ratios. Regardless, this result helps validate the feasibility of the theoretical analysis, and highlights the key benefit of this design: the ML-CoBB converter can be much smaller than the NIBB converter and still deliver similar efficiencies. As the converter is initially demonstrated as a configurable test bed, only the passive component weight can be directly compared. Therefore, considering the specific power in terms of power processed per passive weight, the ratios are 2.58 kW/kg, 7.35 kW/kg, and 14.7 kW/kg for the NIBB, ML-CoBB, and RPI ML-CoBB converters respectively. The performance of the CoBB variants is promising, especially considering that these designs were not optimized for power density, but rather as a proof-of-concept. Furthermore, the 3-level variant only scratches the surface of the potential offered by the multilevel approach, where the benefits are slightly offset by including a second inductor. Higher level counts promise even better power densities, and present an exciting avenue to further explore.

TABLE V: Converter Comparison

Configuration	Peak η [%]	Full Load η [%]	Weight [g]
NIBB Buck	96.9	96.8	388
CoBB Buck	95.4	95.4	136
CoBB RPI Buck	97.3	97.3	68
NIBB Boost	98.0	98.0	388
CoBB Boost	97.5	97.2	136
CoBB RPI Boost	98.1	98.1	68

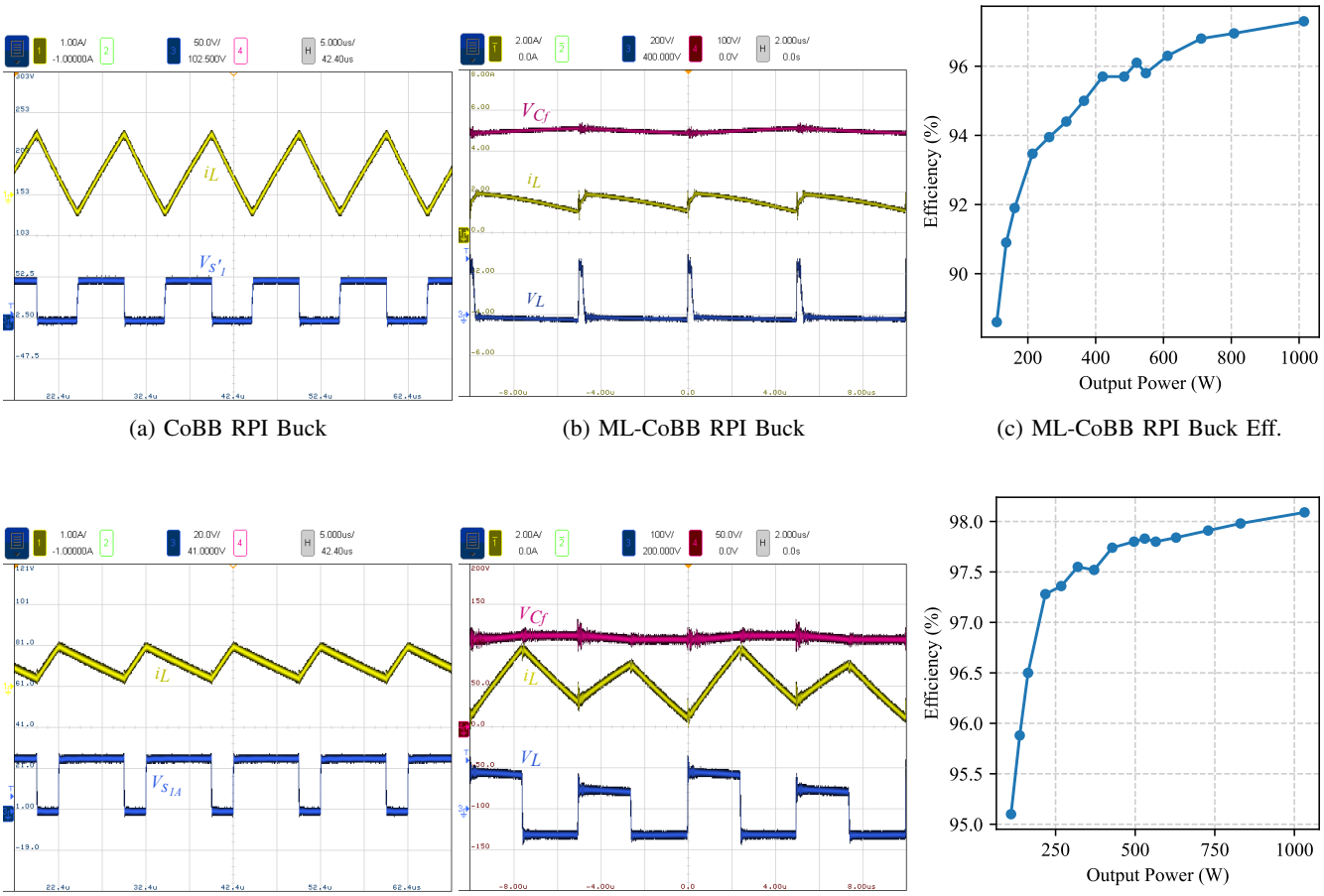

(a) CoBB RPI Buck (b) ML-CoBB RPI Buck (c) ML-CoBB RPI Buck Eff.

(d) CoBB RPI Boost (e) ML-CoBB RPI Boost (f) ML-CoBB RPI Boost Eff.

Fig. 14: Hardware verification for the RPI variants of the CoBB topologies. Operating conditions correspond exactly with those in Fig. 13.

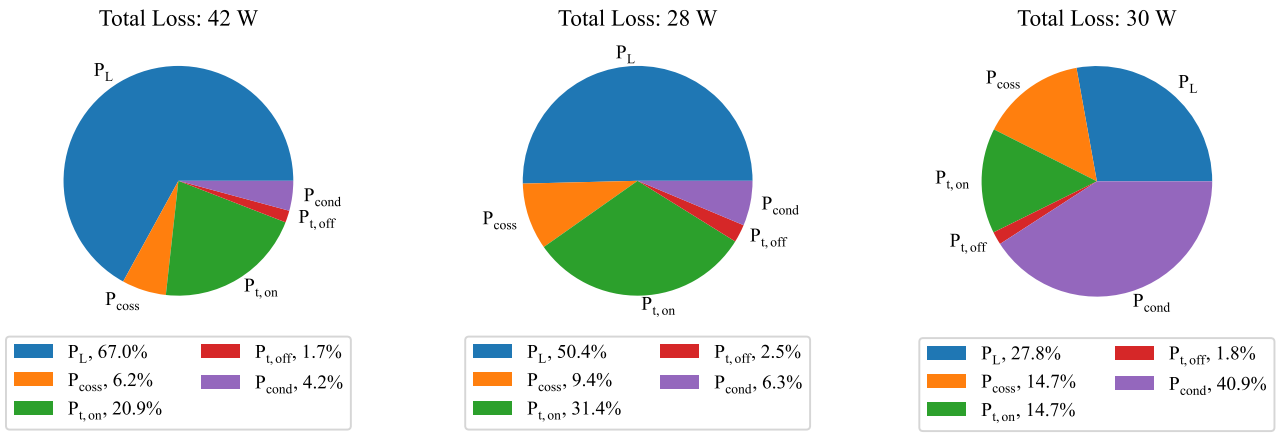

(a) ML-CoBB Loss Breakdown (b) ML-CoBB RPI Loss Breakdown (c) NIBB Loss Breakdown

Fig. 15: Approximate loss breakdown by source for three of the hardware prototypes demonstrated in this work at full load (1 kW) in buck mode (500 V to 270 V).

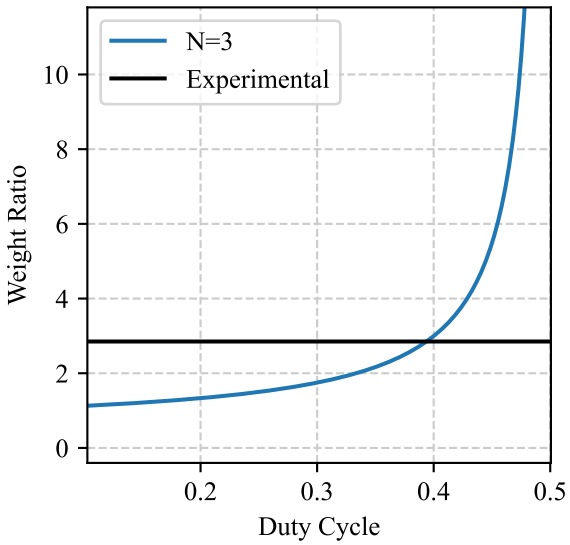

Fig. 16: NIBB converter to ML-CoBB converter passive weight ratio. The $N = 3$ curve is a closer view of the same blue curve in Fig. 10, and the experimental line compares the hardware prototype to its theoretical expectation.

B. Return Path Inductor Topology Variant

The three-level CoBB hardware prototype can be modified to implement the RPI-CoBB and three-level RPI-CoBB variants, and the latter's schematic is shown in Fig. 5. Due to the common-mode voltage induced on the output, this converter variant was tested with discrete resistors as the load, while the previous results presented were tested with an electronic load, in constant resistance mode. However, all other operating conditions and testing conditions were the same as the results presented above.

Figures 14(b) and 14(e) demonstrate successful operation, showing key waveforms in buck and boost mode for 880 W output power. As expected, the current ripple is approximately the same as the three-level CoBB, with half the total inductance. The common-mode voltage induced on the output is equal to the inductor voltage, shown as v_L in the measured waveforms.

Figures 14(c) and 14(f) show the efficiency as a function of output power for the same voltages and conversion ratios as the ML-CoBB converter. The efficiency is higher than measured for the ML-CoBB, and the peak efficiency is not measured before the limit of the test set up was reached. This increase in efficiency and maximum power is due to decreased inductor losses.

C. Approximate Loss Breakdown

Section III presented an analytical framework for comparing the theoretical losses of the different converter topologies detailed in this work. Here the concept of losses is revisited using methods adapted from [30]. Switch parasitic values and inductor manufacturer data were used where possible to provide the most accurate loss contributions for each converter. The breakdowns are shown in Fig. 15 and reiterate two key concepts discussed in Section III. First, the RPI variant of the CoBB converter is more efficient, primarily due to the inductor losses being cut in half; this is consistent with the results in Table V and Fig. 14. Secondly, the difference in relative contribution to total power loss between the CoBB and NIBB converters reflect the main difference in the two topologies: the CoBB topology has an additional inductor, but allows for switches with lower voltage ratings, gate charge, etc. This results in a larger portion of the CoBB converters' loss being attributed to inductor losses P_L, although overall loss, and by extension the measured efficiencies, are close.

V. Control

Experimental measurements presented in Section IV validate the ML-CoBB converter's open loop operation in buck and boost modes. However, for full implementation the converter must be able to seamlessly transition between the two modes without causing imbalance on the flying capacitor. To demonstrate this basic transition between buck and boost modes, a simple PI controller was implemented such that the output voltage was regulated to a constant 270 V, while the input voltage was varied. The controller was implemented digitally using a C2000 microcontroller (MCU), where the output voltage is measured with a resistor divider and fed into the MCU. The error is computed as the difference between the reference voltage V_{ref} and the measured voltage $\bar{v}_{out}$, calculated as a trailing local average. The error in voltage is then fed to a PI controller which determines the required operating mode (buck or boost) and the duty cycle, D.

Figure 17 shows the converter's operation when the output voltage reference is set to 270 V and the input voltage is ramped from 200 V to 460 V over 25 seconds. A deadband was implemented on the duty cycle for boost mode, such that any duty cycle command below 3% is saturated at 3%. The output voltage stays within 10% of the setpoint, while the flying capacitor voltage shows a deviation of less than 30 V. This voltage deviation was suitable for this implementation, as the switch voltages are well overrated. However, further work could decrease the deviation in capacitor voltage with additional complexity or sensing requirements.

Capacitor balancing over a wide regulation and load range is an important consideration for multilevel capacitor-based converters. Future work could implement existing flying capacitor analysis techniques [31], [32], [33] and control strategies to improve capacitor balancing [34], [35], [36], while still maintaining buck and boost capability. Additionally, before practical implementation of the CoBB converter, safe start-up and shutdown must be investigated. Similar to capacitor balancing, start-up [37], [38] and shutdown procedures [39] developed for the FCML converter can be implemented in the CoBB converter without considerable additional complexity.

A. Control Scheme for Unity Conversion

Figure 18(a) depicts the switch states when operating at a unity conversion ratio, $V_{in} = V_{out}$, where no switches

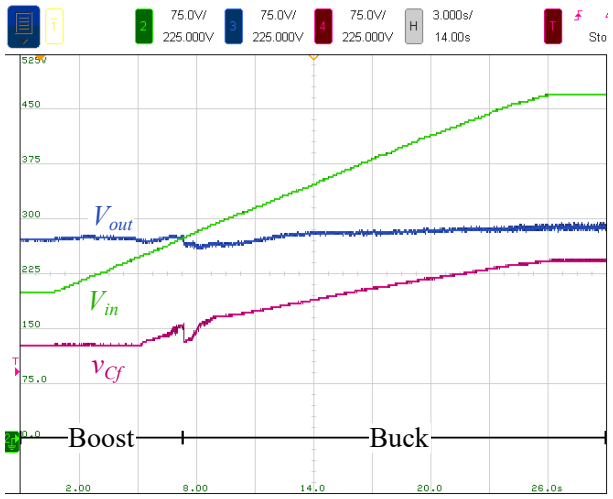

Fig. 17: Measured waveforms verifying closed loop control of the output voltage to 270 V for an input voltage ramp from 200 V to 460 V.

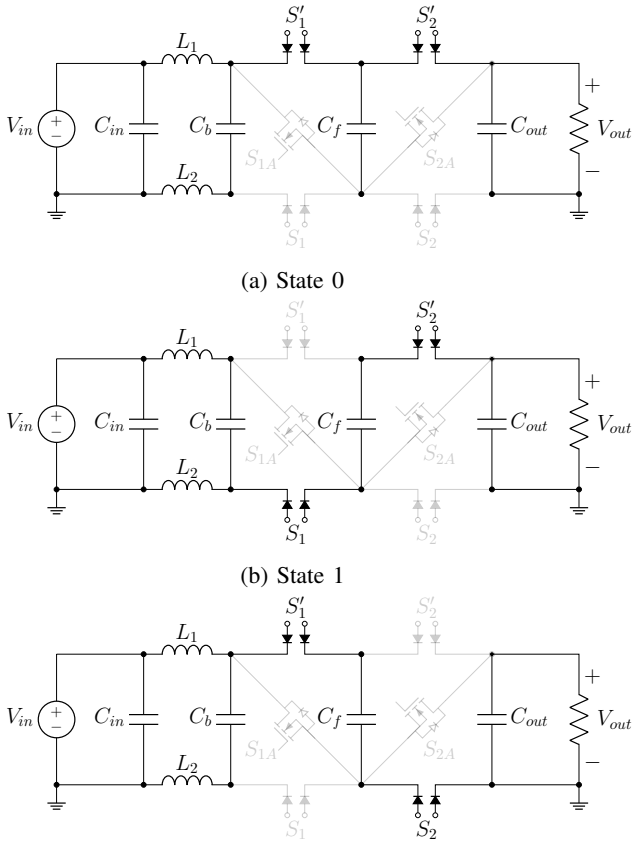

(a) State 0

(b) State 1

(c) State 2

Fig. 18: The different states used in the control scheme for $V_{in} = V_{out}$.

are actively switching and the input and output voltages are directly tied together. As can be seen in Fig. 18(a), this leaves the flying capacitor floating. If the converter remains in this sate, the flying capacitor will subsequently discharge to 0 V at a rate dependent on the parasitic resistances in the circuit. If the flying capacitor deviates from the expected voltage the switches will experience increased switch stress and additional transient stresses when the converter leaves this state and transitions to buck or boost mode. Therefore, if the converter must operate in 1:1 mode for a period of time longer than, or on the same order of magnitude, as the time-constant of the flying capacitor, an active control technique must be implemented to maintain flying capacitor voltage balance. Note, the ML-FCBB converter also requires additional control consideration if operating at unity conversion. Previous work, such as [40], aims to develop control strategies which allow for balanced operation across a wide range of duty cycles. Moreover, high efficiency operation of the NIBB converter near unity conversion has been introduced in previous work [6]. These control strategies differ from the operation described in Section III. There are several methods to ensure capacitor balancing in the CoBB converter; in this work two additional states are added, shown in Figs. 18(b) and 18(c). To ensure that the inductor current ripple is low, state 0 from the original switching scheme is also used.

To determine the duration of each state while maintaining unity conversion ratio, volt-second balance on either inductor can be used. Equation (15) describes the average inductor voltage for V_{L_2}.

$$\langle V_{L_2} \rangle = D_0 \ (V_{out} + V_{in}) + D_1 \ (V_{out} - V_{C_f}) + \ D_2(V_{C_f} - V_{in}) = 0. \quad (15)$$

Parameters D_0, D_1, and D_2 represent the duration of states 0, 1 and 2, respectively. If $D_1 = D_2$, this equation enforces $V_{in} = V_{out}$, independent of the value of D_0. Moreover, given $D_1 = D_2$, and therefore equal time charging and discharging, the flying capacitor voltage remains balanced.

This control scheme was validated experimentally with the three-level CoBB converter operating at $V_{IN} = V_{OUT} = 270\ V$ and 660 W output power. The measured inductor currents and flying capacitor voltage are shown in Fig. 19. The flying capacitor voltage is measured to be 138 V, close to the ideal balanced voltage of 135 V given the operating conditions. This active capacitor balancing technique slightly increases loss, compared to operating the converter with only state 0 at unity conversion. However, the measured efficiency during this 1:1 operation is 98.2%, higher than the efficiencies measured in buck or boost mode, as shown in Fig. 13.

VI. Conclusion

This article presented the condensed buck-boost topology, for efficient and power dense energy conversion in applications requiring both step up and down functionality, as well as bidirectional power flow. The topology is suitable for 2-level and multilevel approaches, and takes advantage of split-inductors and bidirectionally blocking switches to incorporate the FCML design's decreased passive component sizing and switch stress in a compact form. Frameworks were presented for analyzing the losses and passive component requirements, especially as they relate to existing converters with similar applications.

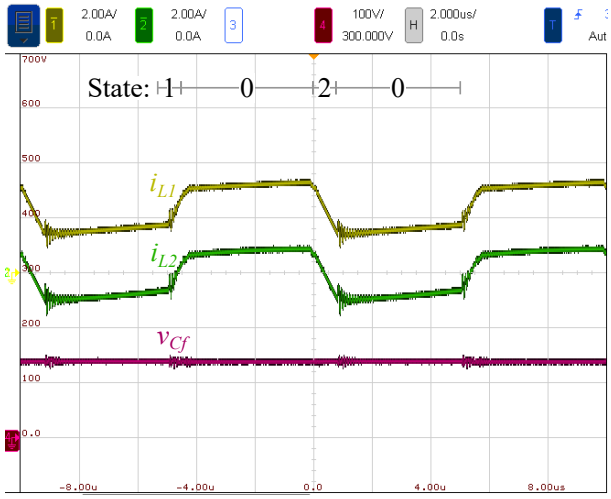

Fig. 19: Measured inductor currents and flying capacitor voltage utilizing active flying capacitor balancing, for $V_{in} = V_{out} = 270$ V and 660 W output power.

Both theory and hardware prototyping demonstrated the ability of the 3-level ML-CoBB converter to process power at similar efficiencies to existing options despite weighing less, and indicate promising potential for even better results with higher level counts. A variation of the implementation utilizing a return path inductor offers the flexibility to exchange inductor volume for common mode voltage, and control schemes were outlined to ensure stable performance across a wide range of operation.

REFERENCES

[1] F. Joseph, G. K. John, and P. P. K, "Solar based two switch buck boost converter with battery as energy storage system for a common dc bus," in *2021 Fourth International Conference on Microelectronics, Signals and Systems (ICMSS)*, 2021, pp. 1–6.

[2] S. Waffler and J. W. Kolar, "A novel low-loss modulation strategy for high-power bi-directional buck+boost converters," in *2007 7th International Conference on Power Electronics*, 2007, pp. 889–894.

[3] H. Ramírez-Murillo, C. Restrepo, T. Konjedic, J. Calvente, A. Romero, C. R. Baier, and R. Giral, "An efficiency comparison of fuel-cell hybrid systems based on the versatile buck–boost converter," *IEEE Transactions on Power Electronics*, vol. 33, no. 2, pp. 1237–1246, 2018.

[4] G. Buticchi, S. Bozhko, M. Liserre, P. Wheeler, and K. Al-Haddad, "On-board microgrids for the more electric aircraft—technology review," *IEEE Transactions on Industrial Electronics*, vol. 66, no. 7, pp. 5588–5599, 2019.

[5] Airbus. (2022, Mar.) Airbus' high-voltage battery technology prepares for ecopulse flight test and beyond. [Online]. Available: https://www.airbus.com/en/newsroom/news/2022-03-airbus-high-voltage-battery-technology-prepares-for-ecopulse-flight-test/

[6] H. Fan, "Design tips for an efficient non-invertering buck-boost converter," *Texas Instruments Analog Applications Journal*, 2014.

[7] T. Meynard and H. Foch, "Multi-level conversion: high voltage choppers and voltage-source inverters," in *PESC '92 Record. 23rd Annual IEEE Power Electronics Specialists Conference*, 1992, pp. 397–403 vol.1.

[8] J. Zou, N. C. Brooks, S. Coday, N. M. Ellis, and R. C. Pilawa-Podgurski, "On the size and weight of passive components: Scaling trends for high-density power converter designs," in *2022 IEEE 23rd Workshop on Control and Modeling for Power Electronics (COMPEL)*, 2022, pp. 1–7.

[9] Y. Zhang, L. Lu, S. M. Ahsanuzzaman, A. Prodić, G. Calabrese, G. Frattini, and M. Granato, "Multilevel non-inverting buck-boost converter with low-frequency ripple-shaping based controller for operating in step-down/step-up transition region," in *2018 IEEE 19th Workshop on Control and Modeling for Power Electronics (COMPEL)*, 2018, pp. 1–7.

[10] D. Menzi, L. Imperiali, E. Bürgisser, M. Ulmer, J. Huber, and J. W. Kolar, "Ultra-lightweight high-efficiency buck-boost dc-dc converters for future evtol aircraft with hybrid power supply," *IEEE Transactions on Transportation Electrification*, pp. 1–1, 2024.

[11] S. Coday, D. Menzi, J. Huber, and J. W. Kolar, "A novel non-mirrored buck-boost flying capacitor multilevel dc-dc converter topology," in *2022 IEEE 7th Southern Power Electronics Conference (SPEC)*, 2022, pp. 1–6.

[12] W. W. Weaver and P. T. Krein, "Analysis and applications of a current-sourced buck converter," in *APEC 07 - Twenty-Second Annual IEEE Applied Power Electronics Conference and Exposition*, 2007, pp. 1664–1670.

[13] R. S. Bayliss and R. C. Pilawa-Podgurski, "An input inductor flying capacitor multilevel converter utilizing a combined power factor correcting and active voltage balancing control technique for buck-type ac/dc grid-tied applications," in *2024 IEEE Workshop on Control and Modeling for Power Electronics (COMPEL)*, 2024, pp. 1–7.

[14] A. Abdulslam and P. P. Mercier, "A battery-connected inductor-first flying capacitor multilevel converter achieving 0.77w/mm2 and 97.1

[15] A. K. Delmar and A. Stillwell, "Current-sourced hybrid switched-capacitor converter for data center power delivery," in *2024 IEEE Applied Power Electronics Conference and Exposition (APEC)*, 2024, pp. 1357–1362.

[16] M. E. Blackwell, A. Stillwell, and R. C. Pilawa-Podgurski, "Dynamic level selection for full range zvs in flying capacitor multi-level converters," in *2018 IEEE 19th Workshop on Control and Modeling for Power Electronics (COMPEL)*, 2018, pp. 1–8.

[17] R. Tymerski and V. Vorperian, "Generation and classification of pwm dc-to-dc converters," *IEEE Transactions on Aerospace and Electronic Systems*, vol. 24, no. 6, pp. 743–754, 1988.

[18] W. W. Weaver and P. T. Krein, "Analysis and applications of a current-sourced buck converter," in *APEC 07 - Twenty-Second Annual IEEE Applied Power Electronics Conference and Exposition*, 2007, pp. 1664–1670.

[19] D. Menzi, J. E. Huber, L. Kappeler, G. Zulauf, and J. W. Kolar, "New return path inductor buck–boost y-inverter motor drive with reduced current stresses," *IEEE Transactions on Power Electronics*, vol. 37, no. 9, pp. 10 086–10 090, 2022.

[20] R. A. Torres, H. Dai, W. Lee, T. M. Jahns, and B. Sarlioglu, "Current-source inverters for integrated motor drives using wide-bandgap power switches," in *2018 IEEE Transportation Electrification Conference and Expo (ITEC)*, 2018, pp. 1002–1008.

[21] M. Guacci, D. Zhang, M. Tatic, D. Bortis, J. W. Kolar, Y. Kinoshita, and H. Ishida, "Three-phase two-third-pwm buck-boost current source inverter system employing dual-gate monolithic bidirectional gan e-fets," *CPSS Transactions on Power Electronics and Applications*, vol. 4, no. 4, pp. 339–354, 2019.

[22] N. Nain, J. Huber, and J. W. Kolar, "Comparative evaluation of three-phase ac-ac voltage/current-source converter systems employing latest gan power transistor technology," in *2022 International Power Electronics Conference (IPEC-Himeji 2022- ECCE Asia)*, 2022, pp. 1726–1733.

[23] S. Bhattacharya, R. Narwal, S. S. Shah, B. J. Baliga, A. Agarwal, A. Kanale, K. Han, D. C. Hopkins, and T.-H. Cheng, "Power conversion systems enabled by sic bidfet device," *IEEE Power Electronics Magazine*, vol. 10, no. 1, pp. 39–43, 2023.

[24] A. Kanale, T.-H. Cheng, R. Narwal, A. Agarwal, B. J. Baliga, S. Bhattacharya, and D. C. Hopkins, "Design considerations for developing 1.2 kv 4h-sic bidfet-enabled power conversion systems," in *2022 IEEE Energy Conversion Congress and Exposition (ECCE)*, 2022, pp. 1–7.

[25] H. Dai, R. A. Torres, F. Chen, T. M. Jahns, and B. Sarlioglu, "An h8 current-source inverter using single-gate wbg bidirectional switches," *IEEE Transactions on Transportation Electrification*, vol. 9, no. 1, pp. 1311–1329, 2023.

[26] J. R. Anderson and M. K. Ranjram, "The harmonically partitioned power converter architecture: Single-stage single-phase ac/dc power conversion using bidirectional switches," *IEEE Transactions on Power Electronics*, pp. 1–14, 2025.

[27] J. T. Stauth, "Pathways to mm-scale dc-dc converters: Trends, opportunities, and limitations," in *2018 IEEE Custom Integrated Circuits Conference (CICC)*, 2018, pp. 1–8.

[28] C. R. Sullivan, B. A. Reese, A. L. F. Stein, and P. A. Kyaw, "On size and magnetics: Why small efficient power inductors are rare," in *2016 International Symposium on 3D Power Electronics Integration and Manufacturing (3D-PEIM)*, 2016, pp. 1–23.

[29] J. A. Oliver, P. Zumel, M. Sanz, C. Raga, D. Izquierdo, O. Garcia, A. Barrado, R. Prieto, R. Azcona, B. Delicado, and J. A. Cobos, "High level decision methodology for the selection of a fuel cell based

power distribution architecture for an aircraft application," in *2009 IEEE Energy Conversion Congress and Exposition*, 2009, pp. 459–464.

[30] T. Modeer, N. Pallo, T. Foulkes, C. B. Barth, and R. C. N. Pilawa-Podgurski, "Design of a gan-based interleaved nine-level flying capacitor multilevel inverter for electric aircraft applications," *IEEE Transactions on Power Electronics*, vol. 35, no. 11, pp. 12 153–12 165, 2020.

[31] Z. Ye, Y. Lei, Z. Liao, and R. C. N. Pilawa-Podgurski, "Investigation of capacitor voltage balancing in practical implementations of flying capacitor multilevel converters," *IEEE Transactions on Power Electronics*, vol. 37, no. 3, pp. 2921–2935, 2022.

[32] N. C. Brooks, R. K. Iyer, R. S. Bayliss, and R. C. N. Pilawa-Podgurski, "Fundamental state-space modeling methodology for the flying capacitor multilevel converter," in *2022 IEEE 23rd Workshop on Control and Modeling for Power Electronics (COMPEL)*, 2022, pp. 1–7.

[33] Z. Xia, K. Datta, and J. T. Stauth, "State-space modeling and control of flying-capacitor multilevel dc–dc converters," *IEEE Transactions on Power Electronics*, vol. 38, no. 10, pp. 12 288–12 303, 2023.

[34] A. Stillwell, E. Candan, and R. C. N. Pilawa-Podgurski, "Constant effective duty cycle control for flying capacitor balancing in flying capacitor multi-level converters," in *2018 IEEE 19th Workshop on Control and Modeling for Power Electronics (COMPEL)*, 2018, pp. 1–8.

[35] J. S. Rentmeister and J. T. Stauth, "A 48v:2v flying capacitor multi-level converter using current-limit control for flying capacitor balance," in *2017 IEEE Applied Power Electronics Conference and Exposition (APEC)*, 2017, pp. 367–372.

[36] R. K. Iyer, I. Z. Petric, R. S. Bayliss, N. C. Brooks, and R. C. N. Pilawa-Podgurski, "A high-bandwidth parallel active balancing controller for current-controlled flying capacitor multilevel converters," in *2023 IEEE Applied Power Electronics Conference and Exposition (APEC)*, 2023, pp. 775–781.

[37] A. Stillwell, C. N. Robert, and Pilawa-Podgurski, "A 5-level flying capacitor multi-level converter with integrated auxiliary power supply and start-up," in *2017 IEEE Applied Power Electronics Conference and Exposition (APEC)*, 2017, pp. 2932–2938.

[38] S. Coday, N. M. Ellis, N. Stokowski, and R. C. N. Pilawa-Podgurski, "Design and flight qualification of a flying capacitor multilevel converter for electric aircraft applications," *IEEE Transactions on Transportation Electrification*, vol. 9, no. 4, pp. 5204–5213, 2023.

[39] S. Coday, N. M. Ellis, and R. C. N. Pilawa-Podgurski, "Modeling and analysis of shutdown dynamics in flying capacitor multilevel converters," *IEEE Transactions on Power Electronics*, vol. 39, no. 8, pp. 9150–9159, 2024.

[40] Y. Zhang, L. Lu, S. M. Ahsanuzzaman, A. Prodić, G. Calabrese, G. Frattini, and M. Granato, "Multilevel non-inverting buck-boost converter with low-frequency ripple-shaping based controller for operating in step-down/step-up transition region," in *2018 IEEE 19th Workshop on Control and Modeling for Power Electronics (COMPEL)*, 2018, pp. 1–7.

Aklilu Aron (Student Member, IEEE) received the B.S. and M.Eng. degrees in electrical engineering and computer science from the Massachusetts Institute of Technology, Cambridge, MA, USA in 2023 and 2024 respectively. He is currently an Applications Engineer at Power Integrations in San Jose, CA, working on efficient power supply design for high voltage power converters. His research interests include novel converter topologies and power electronics applications in renewable power generation and electrification.

Paulin Eliat-Eliat (Student Member, IEEE) received the B.S. and M.S. degree in Energy Engineering from the Catholic University of Louvain (UCLouvain), Louvain-la-Neuve, Belgium, in 2023 and 2025. He was awarded a scholarship from the International Lhoist Berghmans Innovation Chair for a summer internship at Massachusetts Institute of Technology (MIT) in 2024. His research interests include multilevel power converters modeling and control.

Justin Buonato (Student Member, IEEE) is an undergraduate student at at the Massachusetts Institute of Technology studying electrical engineering. Justin plans to graduate with a B.S. in electrical engineering and computer sciences in 2027. Justin's research interests include high performance power converter design and optimization.

Samantha Coday (Member, IEEE) is the Emanuel E. Landsman (1958) Career Development Assistant Professor of Electrical Engineering at the Massachusetts Institute of Technology. Dr. Coday received the B.S. degree in electrical engineering and mathematics from Southern Methodist University, TX, USA, in 2017. She completed the M.S. degree and Ph.D. degree in electrical engineering and computer sciences in 2019 and 2023, respectively, from the University of California, Berkeley, CA, USA. Dr. Coday joined Massachusetts Institute of Technology in 2023 as an Assistant Professor of Electrical Engineering. Her research interests include hybrid switched-capacitor circuits focusing on the design and implementation of converters in harsh aerospace environments. Dr. Coday has received the Outstanding Graduate Student Instructor Award at University of California, Berkeley, the Cadence Women in Technology Scholarship, ThinkSwiss Research Scholarship and the NSF CAREER award.